

# Ionization dynamics of simple metal clusters in intense fields by the Thomas-Fermi-Vlasov method

T. Fennel<sup>1,a</sup>, G.F. Bertsch<sup>2</sup>, and K.-H. Meiwes-Broer<sup>1</sup>

<sup>1</sup> Fachbereich Physik, Universität Rostock, 18051 Rostock, Germany

<sup>2</sup> Department of Physics and National Institute for Nuclear Theory, University of Washington, Seattle, Washington 98195, USA

Received 25 September 2003 / Received in final form 9 December 2003

Published online 16 March 2004 – © EDP Sciences, Società Italiana di Fisica, Springer-Verlag 2004

**Abstract.** The time-dependent response of simple metal clusters to femtosecond laser pulses is investigated using the semiclassical theory based on the Vlasov equation. Starting from a Thomas-Fermi ground state the dynamics are calculated by use of the pseudoparticle method. Systems studied here are sodium clusters containing up to 147 atoms. Both, the energy transfer to the cluster, which is largely affected by the plasmon enhanced absorption, and the following release of energy to the ions are examined in detail. During the laser excitation the feedback of the absorption to the development of the plasmon energy is controlled by competing mechanisms: ionization and cluster expansion. Characteristics of the Coulomb explosion are studied as function of photon energy and cluster size, particularly with regard to the dynamical influence of collective excitations of the electrons. We also predict features in the angular distribution of the ions that could be measured to test the calculated dynamics.

**PACS.** 52.50.Jm Plasma production and heating by laser beams (laser-foil, laser-cluster, etc.) – 36.40.Vz Optical properties of clusters – 36.40.Gk Plasma and collective effects in clusters

## 1 Introduction

The interaction between intense light and matter is a subject of study in disciplines ranging from atomic physics to plasma physics. Among them, the investigation of atomic clusters irradiated with short laser pulses has attracted enormous interest within the last few years. Phenomena like the emission of X-ray radiation as well as the production of highly charged ions have been observed in early experiments [1–3]. Especially the combination of two features make cluster targets extremely appealing for studies in the high intensity regime. While atoms within a cluster feel a bulk-like environment the free cluster itself is completely isolated from energy dissipation to outside matter. Thus a high amount of energy per atom is available for the various decay channels of the cluster. A well-known effect is the complete destruction of strongly excited clusters in an expansion into charged atomic fragments [4]. There is an ongoing discussion about the dominating forces of such a process. The model of a simple Coulomb explosion of a charged system seems to be the proper zero-order approach for small clusters. In case of larger objects the pressure of the hot electron plasma confined in the ionic potential is assumed to dominate the expansion [6]. In the literature this mechanism is often called “hydrodynamic

expansion”. But before the energy can be released to the ionic degrees of freedom it must be transferred from the electromagnetic radiation into the electronic system. Typically the light absorption of clusters is strongly enhanced in comparison to atomic or molecular gases [7]. In particular for metal clusters an additional amplification has been observed experimentally if the photon energy matches the collective dipole mode of the electronic cloud [4,5]. The absorption mechanisms and their efficiency as a function of cluster size and laser frequency is the main subject of this work.

Within the broad spectrum of methods for the description of clusters in intense fields a compromise has to be found. Unless quantum features are totally omitted classical models combined with parameterized rates for ionization and recombination can handle multiple active electrons per atom as used for rare gas clusters [8,9]. Here we rely on a more sophisticated time-dependent technique to resolve the fermionic character of the electrons under nonlinear excitation that restricts the number of active electrons strongly.

The influence of the coupled motion of ionic and electronic components and the importance of collective excitations are of particular interest in the present study. To get a comprehensive insight into the underlying mechanisms we have carried out full three-dimensional simulations to

---

<sup>a</sup> e-mail: thomas.fennel@physik.uni-rostock.de

describe the dynamics of sodium clusters irradiated with visible linearly polarized light at  $I = 10^{11}$  W/cm<sup>2</sup>.

The resulting many-body problem is treated with a semiclassical mean-field approximation of time-dependent density-functional theory coupled to classical motion of atomic ions using pseudopotentials. We will denote the method as Thomas-Fermi-Vlasov molecular dynamics (TFV-MD). The technique is capable to deal with clusters containing hundreds of atoms excited in the highly nonlinear regime.

Comparable Vlasov models have already been used extensively to describe nonlinear excitations of sodium clusters within the jellium approximation [10,11], as well as with ionic pseudopotentials to resolve the ionic response [12,13].

However, up to now there was no systematic exploration of cluster sizes and the dynamics of the cluster destruction and its transformation into an expanding vapor of ions. In this work we examine the dependencies on cluster size and laser frequency while following in detail the energy flows leading to the final state.

To reach a high numerical performance we use the pseudoparticle method to represent the electron distribution function, together with the very efficient method to solve Poisson's equation, the iterative multigrid algorithm [14]. We thereby achieve a linear scaling with system size for the computational costs of the electronic propagation.

## 2 Method

### 2.1 Vlasov propagation

Among the methods for the quantum description of many-particle dynamics, the time-dependent density functional theory (TDDFT) offers a tractable computational framework for treating electronic systems. The propagation can be decoupled into a set of  $N_e$  equations for the Kohn-Sham orbitals evolving in a self consistent field [15],

$$i\hbar \frac{\partial}{\partial t} \phi_i(\mathbf{r}, t) = \left( -\frac{\hbar^2}{2m} \Delta + V_{\text{eff}} \right) \phi_i(\mathbf{r}, t)$$

$$V_{\text{eff}} = V_{\text{ion}} + V_{\text{laser}} + V_{ee}(n_e) + V_{xc}(n_e). \quad (1)$$

Here the effective potential  $V_{\text{eff}}$  contains the external fields, the electron Hartree potential and an additional contribution containing exchange and correlation effects. In the classical limit ( $\hbar \rightarrow 0$ ) equation (1) can be approximated by the Vlasov equation, which describes the evolution of the classical one-body phase-space distribution in the same potential,

$$\frac{\partial}{\partial t} f(\mathbf{r}, \mathbf{p}, t) = \nabla_r V_{\text{eff}}(\mathbf{r}, t) \cdot \nabla_p f(\mathbf{r}, \mathbf{p}, t) - \frac{\mathbf{p}}{m} \cdot \nabla_r f(\mathbf{r}, \mathbf{p}, t). \quad (2)$$

As the Vlasov propagation is close to the quantum, it is a convenient tool to investigate dynamical problems when

the specifically quantum aspects such as energy gaps are not needed. Especially in the case of highly nonlinear excitations the missing quantum effects don't play a noticeable role. Also, the Vlasov theory automatically respects the conservation laws, which are realized by the sum rules in the linear response regime.

### 2.2 Pseudoparticle method

The direct propagation of the particle distribution  $f(\mathbf{r}, \mathbf{p}, t)$  would require the treatment of a time-dependent gridded function in six dimensions, which is too demanding even for modern computers. A more practical technique is to represent the distribution function by a set of pseudoparticles. We thus approximate the distribution function by

$$f(\mathbf{r}, \mathbf{p}, t) = \frac{1}{N_s} \sum_{i=1}^{N_{pp}} g_r(\mathbf{r} - \mathbf{r}_i(t)) g_p(\mathbf{p} - \mathbf{p}_i(t)),$$

where  $N_{pp}$  is the number of pseudoparticles, each characterized by its phase space coordinates  $(\mathbf{r}_i, \mathbf{p}_i)$ . The extensions of the pseudoparticles in position and momentum space are represented by the functions  $g_r$  and  $g_p$ . Each electron will be represented by a large number of pseudoparticles,  $N_s$ , so the total number satisfies  $N_{pp} = N_s N_e$ .

The Vlasov equation is then mapped onto a problem in Newtonian physics, propagating the pseudoparticles in some potential field. The smoothing functions are taken to be Gaussians,

$$g_r(\mathbf{r}) = \frac{1}{\pi^{3/2} d_r^3} \exp(-r^2/d_r^2)$$

$$g_p(\mathbf{p}) = \frac{1}{\pi^{3/2} d_p^3} \exp(-p^2/d_p^2)$$

where  $d_r$  and  $d_p$  are the width parameter. In this work we choose  $d_r = 1.15$  Å. The explicit specification of the momentum width parameter  $d_p$  is not necessary here. For the dynamical propagation the electronic contributions of the mean-field potential are determined by the electron densities on a spatial grid ( $d_{\text{mesh}} = 1.0$  Å). From the positions of the pseudoparticles  $\mathbf{r}_i$  the real-space density  $n_e = \int f(\mathbf{r}, \mathbf{p}, t) d^3p$  at grid points  $r$  is given by

$$n_e(\mathbf{r}) = \frac{1}{N_s} \sum_i^{N_{pp}} g_r(\mathbf{r}_i - \mathbf{r}). \quad (3)$$

The resulting density  $n_e$  is used directly to construction the DFT potential field,

$$V_{\text{eff}} = V_{\text{ext}}(\mathbf{r}, t) + V_{ee}(n_e(\mathbf{r}), t) + V_{xc}(n_e(\mathbf{r}), t).$$

Considerable computational effort is required to calculate the Hartree potential  $V_{ee}$ . This is done by solving the Poisson equation, which can be done efficiently using the multigrid-method. The multigrid algorithm is very appealing for huge systems because it scales linearly with system

size. In this work, the size of the grid cube is  $129^3$  mesh points. The pre-conditioning of the boundaries is done by a multipole expansion up to the quadrupole which scales linearly too. For the exchange we have used the LDA approximation of the free electron gas while the correlation parametrization is taken from reference [16],

$$V_{xc}(\mathbf{r}) = -\frac{e^2(3\pi^2)^{1/3}}{4\pi^2\epsilon_0}n_e^{1/3}(\mathbf{r}) - 0.90576 \text{ eV} \times \ln\left(1 + \frac{11.4}{r_s(\mathbf{r})}\right) \quad (4)$$

where as usual  $r_s(\mathbf{r}) = (3/4\pi a_0^3 n_e(\mathbf{r}))^{1/3}$ . The dynamics is determined by the following Newtonian equations of motion,

$$\dot{\mathbf{r}}_i = \frac{\mathbf{p}_i}{m_i} \quad \dot{\mathbf{p}}_i = -\int V_{eff}(\mathbf{r}) \nabla_{\mathbf{r}_i} g_r(\mathbf{r} - \mathbf{r}_i) d^3\mathbf{r}.$$

The acceleration equation may be derived from the DFT energy function (Eq. (5)) below used also for the static solutions. The  $V_{xc}$  here and the  $E_{xc}$  in the functional are related by  $E_{xc}(n) = \int_0^n dn' V_{xc}(n')$ . Note that the pseudoparticles interact with an extended charge distribution given by the function  $g_r$ .

The numerical time integration of the pseudoparticles is done by the Verlet algorithm [17] which is time-reversible and achieves second-order accuracy with only one force evaluation per time step. For the simulations we have used typically a time step of  $\delta t = 0.025$  fs. This step size ensures conservation of the total energy with insignificant noise. Finally, the single-particle energies may be calculated from the single-particle Hamiltonian

$$h_i = \frac{\mathbf{p}_i^2}{2m_i} + \int V_{eff}(\mathbf{r}, t) g_r(\mathbf{r} - \mathbf{r}_i) d^3\mathbf{r}.$$

### 2.3 Ground state preparation

A static theory is needed to find the initial pseudoparticle distribution for the dynamical model. We use here the Thomas-Fermi ground state at zero temperature [18, 19]. The Thomas-Fermi theory is the simplest approximation to a DFT for fermionic systems, taking the local density approximation for both the kinetic and potential energies. The kinetic energy is calculated as that of the homogeneous electron gas. Up to the Fermi energy all momentum states are occupied with two electrons according to the Pauli principle. Note that the discrete pseudoparticle density is used to define the kinetic energy. The total energy is given by the functional

$$E_{tot} = \int \left[ \frac{3}{10} \frac{\hbar^2(3\pi^2)^{2/3}}{m} n_\delta^{5/3}(\mathbf{r}) + V_{ions}(\mathbf{r}) n_e(\mathbf{r}) + \int \frac{e^2}{4\pi\epsilon_0} \frac{n_e(\mathbf{r}')}{|\mathbf{r} - \mathbf{r}'|} d^3\mathbf{r}' n_e(\mathbf{r}) + E_{xc}(n_e(\mathbf{r})) \right] d^3\mathbf{r}. \quad (5)$$

To find the ground state, the total energy has to be minimized for a given number of electrons  $N_e$ . Thus the

variational problem contains a Lagrange multiplier, the chemical potential  $\mu$ , to meet this constraint. From the optimized density the pseudoparticle positions are sampled while their momenta are chosen isotropically within a local Fermi sphere

$$\frac{dn}{dp} = \frac{p^2}{\hbar^3 \pi^2}, \quad p_f(\mathbf{r}) = \left( 2m_e \left[ \mu - \int g_r(\mathbf{r} - \mathbf{r}') V_{eff}(\mathbf{r}') d^3\mathbf{r}' \right] \right)^{1/2}. \quad (6)$$

According to equation (6) the phase-space density up to the chemical potential is constant at all occupied parts of space, namely two electrons per state. While the pseudoparticles themselves are moving during the propagation the distribution function  $f(\mathbf{r}, \mathbf{p}, t)$  does not change since the right side of equation (2) vanishes if there is no external perturbation. Thus the Thomas-Fermi ground state is a static solution of the Vlasov equation and is suitable for the pseudoparticle initialization.

### 2.4 Ground-state stability

Because interactions between particles in the ensemble are absent, the Vlasov equation respects Liouville's theorem and conserves phase space density. However, the pseudoparticle implementation of the Vlasov equation introduces numerical noise through the density sampling. As a consequence there are spurious interactions between the pseudoparticles which will drive the system away from the Fermi-Dirac distribution towards the classical Boltzmann equilibrium. Particles will scatter to states above and below the Fermi surface, leading to a phase space occupation greater than one for deeply bound electrons and evaporation of electrons from the high energy tail. Much effort has been invested to overcome this problem by including Pauli blocked dynamical correlations [20–24]. For the pure Vlasov propagation the thermalization time can be qualitatively estimated with

$$\tau \propto \frac{p}{n_e} d_r^4 N_s, \quad (7)$$

where the physical quantities  $p$  and  $n_e$  are electronic momentum and density, and the numerical parameters  $d_r$  and  $N_s$  are the spatial smearing and the pseudoparticle scaling [25]. If we approximate  $p$  with the Fermi momentum of the free-electron gas ( $p_f^3 = 3\hbar^3 \pi^2 n_e$ ), the density cancels out. Thus, we obtain an expression for the relaxation time depending only on numerical parameters

$$\tau \propto d_r^4 N_s. \quad (8)$$

According to equation (8) the relaxation can be suppressed effectively by increasing the pseudoparticle width. Unfortunately this parameter has to be chosen to match the system properties. Hence the brute force way to keep the system “fermionic” as long as possible is the increase of the pseudoparticle scaling  $N_s$ . In the present work  $N_s$

**Table 1.** Scaling and width-parameters of the Gaussians defining the optimized sodium pseudopotential. The total charge  $c_1 + c_2 = 1$  is fixed by the number of active electrons per atom.

$c_1$	$a_1$	$c_2$	$a_2$
-0.8	0.85 Å	1.8	1.15 Å

is determined by checking the ground-state stability considering a typical system. As a good compromise between thermal relaxation and computational costs we have used  $N_s = 10000$  pseudoparticles per electron which allows us to follow the propagation up to picoseconds without too much influence of the thermalization. A more detailed analysis of the autorelaxation of the ground state is given in Section 3.1.

## 2.5 Ionic pseudopotentials

As in the quantum DFT, the ionic potentials and the effects of core electrons must be approximated by pseudopotentials that are smooth and only act on valence electrons. The alternative, an all-electron treatment of the dynamics, would require treatment of fast and strongly localized particles and would increase the costs of computation enormously. In the present study on sodium we only treat a single electron per atom explicitly,  $N_e = N$ .

There is considerable freedom in the choice of pseudopotentials. Here we use a sum of Gaussians to represent the effective charge distribution associated with the ions,

$$\rho_{ion}(r) = \sum_{n=1}^k c_n \frac{e}{\pi^{3/2} a_n^3} \exp(-r^2/a_n^2).$$

The  $c_n$  are the charges associated with each Gaussian; in general

$$Q_{ion} = \sum_{n=1}^k c_n,$$

and in the present study  $Q_{ion} = 1$ . The electric field for such a potential can be expressed in terms of the error function as

$$V_{ion}(r) = - \sum_{n=1}^k c_n \frac{e^2}{4\pi\epsilon_0 r} \operatorname{erf}(r/a_n).$$

For the present study we take two Gaussians to parameterize the pseudopotential. The free parameters are chosen to fit selected spectroscopic properties of sodium. Here we have optimized the ionization potential, the atomic polarizability and the dimer bond length (from Ref. [26]). The parameters of the pseudopotential are given in Table 1 and the calculated properties are compared with the reference data given in Table 2. One sees that the two-Gaussian parameterization leads to model properties close to the reference data, except the binding energy of the dimer.

**Table 2.** Calculated atomic and molecular properties for the sodium pseudopotential compared to reference data taken from [26]. Note that calculated values are only valid for the particular pseudoparticle width of  $d_r = 1.15$  Å.

		this work	reference
ionization potential	[eV]	5.30	5.13
atomic polarizability	[Å <sup>3</sup> /4πϵ <sub>0</sub> ]	21.9	23.6
dimer bond length	[Å]	3.739	3.714
dimer binding energy	[eV]	0.235	0.763

However, for our present purposes to study the dynamics in strong laser fields, the errors should not be significant as long as the initial bond length was adjusted to the proper value. For a given cluster size the geometrical ground-state configuration of the ionic frame is calculated by the energy-minimization via stimulated annealing.

The dynamical propagation of the ions is forced by the interaction with all other ions and the electronic density. For the interionic forces only the asymptotic charges are used to ensure a strong repulsion between approaching ions. Finally the time integration of the ionic trajectories is done by a modified Verlet algorithm

$$\begin{aligned} \dot{\mathbf{R}}_i &= \frac{\mathbf{P}_i}{M_i} \\ \dot{\mathbf{P}}_i &= -\nabla_{\mathbf{R}_i} \left[ \sum_{i \neq j} \frac{1}{4\pi\epsilon_0} \frac{Q_i Q_j}{|\mathbf{R}_i - \mathbf{R}_j|} \right. \\ &\quad \left. + \int V_i(|\mathbf{R}_i - \mathbf{r}|) n(\mathbf{r}) d^3 r \right]. \end{aligned}$$

The charge-to-mass ratio of the ions is much lower compared to the electrons. Hence many electronic time steps can be performed between two updates of the ionic system. Here the ions are updated after 20 steps of pseudoparticle propagation, i.e. all 0.5 femtoseconds. During the electronic propagation the density is averaged to minimize numerical noise within the force on the ions.

## 2.6 Observables

The main goal of the dynamical simulation is to track the development of the energy absorption, ionization and spectral properties of the collective modes. For the calculation of kinetic and potential energy contributions all particles within the simulation box are taken into account. If pseudoparticles reach the boundary they are taken out of the simulation and appear as inactive particles in the ionization of the system. The dipole moment of the active particles is calculated as a marker of the collective excitations. To measure the spectral properties of the dipole mode the free response is evaluated after an impulsive excitation by giving all pseudoparticles a constant initial velocity offset.

## 2.7 Numerical aspects

As already mentioned all algorithms used for the electronic propagation possess a linear scaling with system size. Thus a scaling law for the computational costs can be given in dependence of the size of the arena ( $N_g$ : number of grid points) and the number of pseudoparticles used in the simulation ( $N_{pp} = N_e N_s$ ). Here we want to give an estimation of the floating point operations (fpo) necessary for one time step. The most demanding tasks that will rule the numerical costs are the pseudoparticle sampling and the Poisson solver. Each injection of a pseudoparticle into the density function or a readout of one scalar property requires a folding operation with the smoothing function  $g_r$ . Here the folding is done within a box of  $N_f^3$  points that encloses the smearing function. In the present study we use a folding-box length of  $N_f = 7$ . Therefore one folding operation requires at least 343 evaluations of the smoothing function and the same number of operations to make an injection or a readout. All in all 6 folding operations are necessary per pseudoparticle and time step, one injection and five readouts (3 force components, single particle energy and mean-field energy).

The second demanding part is the multigrid routine of the Poisson solver that requires about  $200N_g$  floating point operations for one full process. The number of operations roughly required for a time step is then

$$N_{fpo} = 12N_{pp} N_f^3 + 200 N_g.$$

In a typical calculation using  $N_g = 129^3$  grid points and  $N_{pp} = 147 \times 10^4$  pseudoparticles a time step requires about  $6.5 \times 10^9$  floating point operations. A fast computer should be able to do this within a few seconds, but the speed is dramatically affected by memory latencies. In our case the parallelized MPI-program has to be launched on 6 processors (IBM p690) to do a time step in less than 6 seconds. A significant speedup would be possible if a huge cache memory were available.

## 3 Results

### 3.1 Cluster geometry and numerical stability

The investigated systems are  $\text{Na}_N$ -clusters with sizes of  $N = 13, 55, 147$ . Here the ionic ground-state relaxation results in icosahedral configurations, shown in Figure 1. Since the semiclassical model ignores spin effects and energy gain due to deformation the resulting structure is strongly dominated by geometrical shells effects of the ions. This will slightly modify the optical properties as some structural features known from more sophisticated quantum calculations are absent [27, 28]. However, for the investigation of the interaction mechanisms of clusters with intense laser pulses no significant influence is expected by small deviations of the cluster configuration.

To demonstrate the long-time stability and the magnitude of thermalization effects the dynamical propagation of  $\text{Na}_{147}$  is performed without external perturbation for

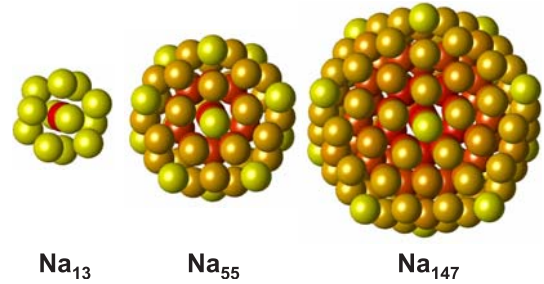


**Fig. 1.** Optimized ionic structures for investigated sodium clusters. The sizes correspond to icosahedral structures with closed geometric shells.

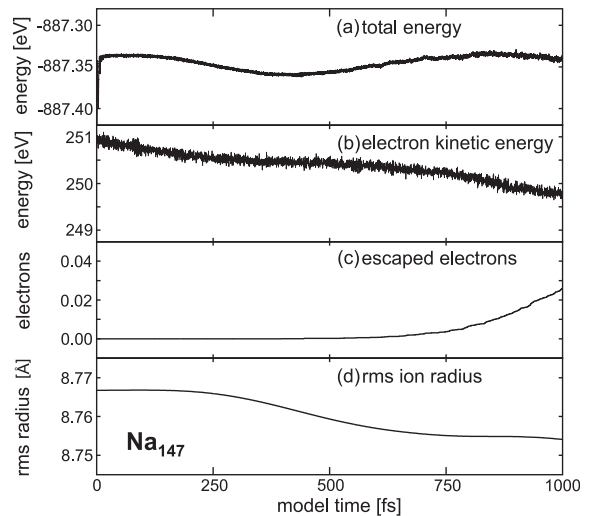


**Fig. 2.** The ground state of  $\text{Na}_{147}$  is evolved in time for one picosecond to check the stability of observables during propagation. The total energy in the top panel (a) shows a slow oscillation from the ionic propagation, together with a small noise ( $\leq 5$  meV). The total error is less than 20 meV. However, one sees a small loss of electronic kinetic energy (b), as a spurious autoionization (c), corresponding to a classical thermalization. The ionic rms (d) shows only a small deviation from the initial value.

one picosecond. The results are analyzed in two ways:

- check of the time development of theoretically constant observables, namely total and kinetic energy, charge and cluster radius (Fig. 2);
- direct comparison of initial and the final state by checking the mean-field potential and the single-particle energy occupation (Fig. 3).

An important requirement for the validity of the numerical model is the conservation of the total energy in the system. For the given parameters the total energy in the Figure 2a shows a total error of less than 20 meV within 1 ps of integration. While high frequency noise ( $\leq 5$  meV) is induced by the electronic propagation, the slow oscillation comes from the trajectory solver for the ionic components. As a typical thermalization effect the total kinetic energy of the electrons decreases in time due to the occupation of lower energy states. Here the energy loss of less than 0.5% is not dramatic, Figure 2b.

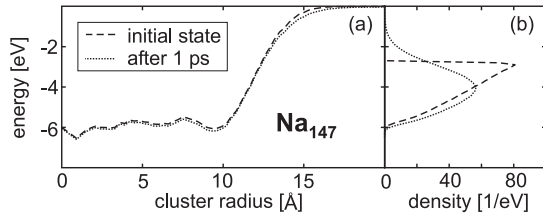


**Fig. 3.** The radially averaged mean-field potential (a) and the occupation of single particle states (b) are compared for the initial and the propagated groundstate of  $\text{Na}_{147}$ . During the time evolution the potential remains almost static. For the single-particle states, all electronic states are initially fully occupied up to the chemical potential at  $\mu = -2.7$  eV. Due to the classical thermalization, the distribution starts to violate the Pauli principle for low energies and a spurious formation of the classical Boltzmann tail at higher energies takes place, as well as emission of particles into the continuum (not shown).

Another effect of thermalization is a spurious autoionization which results in a total electron loss of 0.04 electrons within the first picosecond, seen in Figure 2c. Numerical noise and the mentioned changes in the electronic system also induce a rearrangement of the ionic geometry, but the effect is rather small. The rms-averaged radius of the ions is shifted downwards by less than 0.2%, as may be seen in Figure 2d.

A direct comparison of the changes within the mean-field potential and the single particle occupation is shown in Figure 3. The radial potential is very stable during the propagation. As a consequence of thermalization the occupation in energy space is slightly shifted towards a classical Boltzmann distribution.

### 3.2 Linear response

Before applying a strong laser field it is instructive to examine the optical response in the linear regime. For the systems under study the laser will dominantly couple into the dipole mode as the wavelength is well above the cluster diameter. All key features of resonances and the power absorption in the regime of small excitations can easily be extracted from the dynamic polarizability. The results can then serve as a guideline and a first estimate of the light absorption for the higher intensity regime. We calculate the linear response using the real-time method in which the time evolution of observables is recorded after an impulsive excitation. Starting from the ground state the dipole moment is tracked for 250 fs after all electrons where given a constant velocity offset of  $\Delta v = 1 \text{ \AA}/\text{fs}$  as a gentle perturbation. In Figure 4a the decay of the dipole oscillation is plotted for  $\text{Na}_{147}$ . The absorption cross-section is then derived from the Fourier transform of the dipole signal as shown in Figure 4b. One sees a strong collective excitation in all the clusters, peaked just below 3 eV. This is the well-known surface plasmon, and its position accords with earlier studies and the results of quantum TDLDA calculations [20]. The energy and life times for the collective modes are given in Table 3. With

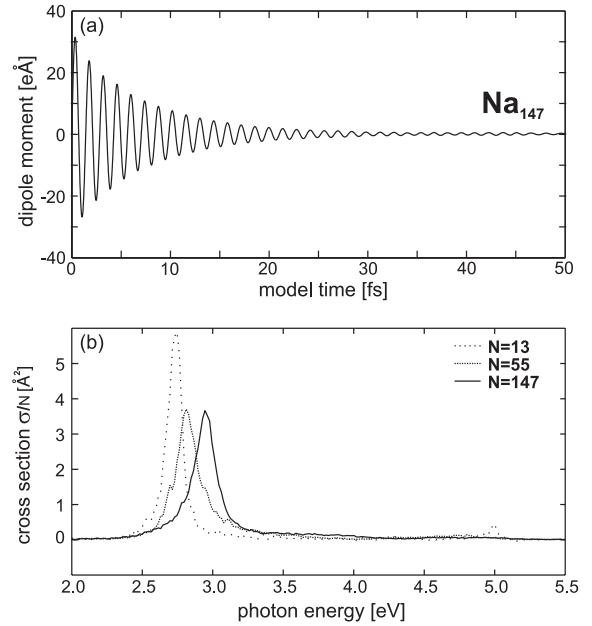


**Fig. 4.** (a) Example for the decay of the dipole moment for  $\text{Na}_{147}$  after initial excitation of all electrons by a constant velocity offset. (b) Calculated linear response light absorption cross-section for  $\text{Na}_N$  clusters normalized by the number of atoms. The strong maximum below 3 eV corresponds to the surface plasmon. In all three spectra the TRK-sum-rule is fulfilled and more than 99% of the oscillator strength are within the plotted region.

**Table 3.** Calculated surface plasmon properties for the dipole mode.

	$\text{Na}_{13}$	$\text{Na}_{55}$	$\text{Na}_{147}$
plasmon energy [eV]	2.74	2.82	2.95
life time [fs]	11.1	6.97	6.90

increasing cluster size the plasmon energy is blue-shifted towards the classical Mie value of 3.49 eV due to the decreasing influence of the surface effects and electron-spill-out.

The TFV spectrum has a continuous envelope, unlike the fully quantum spectra which consist of discrete lines. The observed damping and the consequent spectral width is not present in the more simplified jellium model. We conclude, in agreement with reference [29], that the lifetime is due to electron-ion scattering and is not a numerical effect of the simulation.

### 3.3 Nonlinear excitation

In the following, we study the dynamics when the system is excited by an intense laser field. Since the cluster sizes are small, the dipole approximation is valid and we may treat the laser field as a spatially uniform electric field. Simulations are performed with laser frequencies from below to above the plasmon frequency, in the range  $\hbar\omega = 2.3\text{--}3.5$  eV. Following reference [12], the used pulse

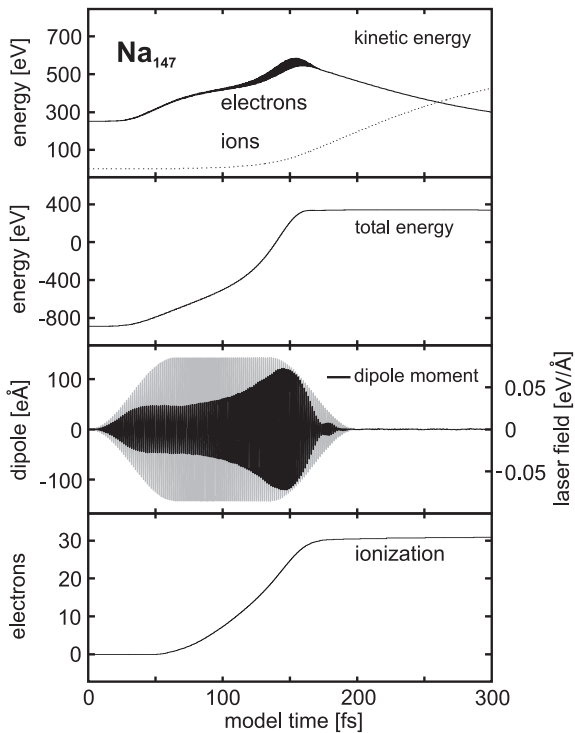


**Fig. 5.** Time dependent observables during the excitation of  $\text{Na}_{147}$  by a 200 fs laser pulse of  $I = 10^{11} \text{ W/cm}^2$  at a photon energy of  $\hbar\omega = 2.8 \text{ eV}$ . The development of kinetic energies of electrons and ions, the total system energy, the dipole moment as well as the cluster charge are shown. Note that within the plot for the dipole moment the envelope of the laser field is sketched in gray.

shape is in the form of a sine squared for the rising and falling edges embedding a 70 fs constant section. The total pulse length is 200 fs and the peak intensity is taken to be  $10^{11} \text{ W/cm}^2$  which corresponds to a peak field strength of  $E_{\text{peak}} = 0.086 \text{ eV/\AA}$ .

To discuss a typical example first we show the results for  $\text{Na}_{147}$  excited with a photon energy of  $\hbar\omega = 2.8 \text{ eV}$ , where the laser frequency is just below the plasmon frequency of the initially cold cluster. The envelope of the exciting field, starting at  $t = 0$ , is shown on the third panel of Figure 5 in gray. The top panel shows the electron kinetic energy, which increases during the laser irradiation and decreases afterwards. The maximum rate of increase happens at  $t = 150 \text{ fs}$ , the point where the plasmon frequency of the expanding cluster matches the laser frequency. One may notice also a steep increase in the total energy at that time (second panel of Fig. 5), and a large dipole amplitude in the electronic oscillation (third panel). To obtain frequency matching a shift of the plasmon energy down to the laser photon energy is required, discussed in more detail in the next section. The ions acquire relatively little kinetic energy during the radiation period, top panel of Figure 5. Following that, however, there is a strong increase in the ion kinetic energy, much of which is by transfer from the electron kinetic energy. This can be understood as follows. At the termination of the laser pulse at  $t = 200 \text{ fs}$ , the clus-

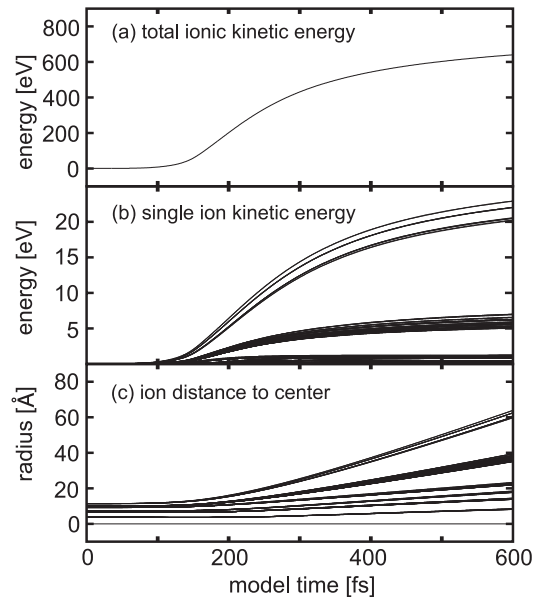


**Fig. 6.** Total (a) and single (b) ion kinetic energy during the explosion of  $\text{Na}_{147}$  after excitation at  $\hbar\omega = 2.8 \text{ eV}$ . The bottom panel shows the development of the ion distance to the center of mass of the cluster.

ter is already ionized in a high charge state, bottom panel of Figure 5. The resulting Coulomb potential couples the remaining electrons strongly to the ions. Energy sharing readily takes place under these circumstances. In hydrodynamic terms, the electrons exert thermal pressure on the Coulomb well, losing their momentum there and accelerating the ions until the cluster has decomposed into separated atomic fragments. From that point on only the electrostatic repulsion of the charged system is effective to accelerate the ions, and the system disassembles by a Coulomb explosion.

At first glance the run of the total ion kinetic energy on the top panel in Figure 6 looks very close to results of a pure Coulomb explosion as was described in reference [30]. A symmetrical destruction would be expected from that classical approach. Indeed we find a shell by shell expansion of the cluster as shown by the distance-to-center-plot within Figure 6c, but the initially sharp shells start to wash out significantly. This becomes even more obvious from the single ion kinetic energy plot in Figure 6b. The divergence is due to the stronger repulsion of ions sitting along the polarization axis of the laser, as can be seen from the angle resolved ion kinetic energy spectra shown in Figure 7a. Here the two outermost shells have clearly separated energy bands which are overlaid with the angle dependent enhancement due to the polarization effect.

A high fraction of the kinetic energy is given to the surface ions. For the example of  $\text{Na}_{147}$  the outermost subshell of the icosahedral structure contains 12 atoms, together carrying more than 50% of the total amount. Most of the residual energy is given to the next subshell while the inner ions remain practically at rest.

From the charge distribution of the ionic fragments the contribution of the electrostatic repulsion to the cluster

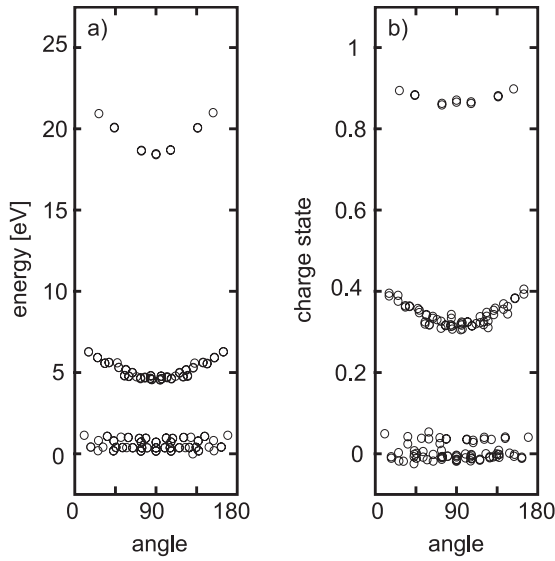


**Fig. 7.** Angle resolved single particle kinetic energy (a) and charge state (b) of the atomic fragments after excitation of  $\text{Na}_{147}$  using the laser parameters of Figure 5. The data points correspond to a model time of  $t = 500$  fs, angles are given with respect to the laser polarization axis.

explosion can be analyzed. To determine the ionic charges all the pseudoparticles still in the arena at  $t = 500$  fs are assigned to the closest ion. This is late enough so that practically all unbound pseudoparticles have already left the arena. Each pseudoparticle carries a fraction of an electron charge and the total charge must be interpreted as a statistical average. The resulting spectra, shown in Figure 7, show a strong shell signal, with the outer ions in higher charge states, analogous to the charge on a classical conducting sphere, which is localized on the surface. Also contributing, the high field gradient at the cluster surface, which promotes field ionization of the outer ions, while the inner region is more screened. The field ionization should be most effective on the ions located where the surface is perpendicular to the laser polarization axis, and indeed a slight angular enhancement can be seen in Figure 7b.

To analyze the evolution of the disassembly phase in more detail, the observed energetics are compared with classical Coulomb dynamics. Let us assume that the ions acquire their final charges by  $t = 0$  fs. The ionic potential energy may then be calculated from their positions as given in Figure 6c and their charges from Figure 7b. The resulting potential function is shown in Figure 8, together with the kinetic energy and their sum. We see by the constancy of the total energy that a classical Coulomb explosion describes the energetics very well for times later than 350 fs. However, there is a significant transfer of energy from the electrons to the ions between  $t = 100$  and 350 fs. One possibility to explain an increase of energy in this period is that the ions may be in a higher charge state just after the laser irradiation. That would increase the initial potential energy. However, this explanation is only tenable if the ions are able to capture electrons during the expansion phase.

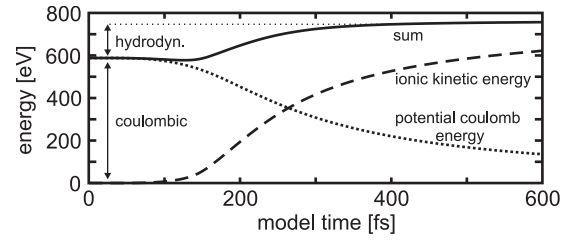


**Fig. 8.** The time-dependent potential, kinetic and total classical energy of the ionic frame during the expansion of  $\text{Na}_{147}$  corresponding to Figure 5 is shown. To calculate the potential and total energy the final charge distribution among the ions has been used while true trajectories and kinetic energies are taken from the model. If the ion dynamics is only driven by pure Coulomb forces the total energy should remain constant. The gain of the total Coulomb energy between 150–400 fs is due to a release of  $\sim 165$  eV thermal energy from the hot electron gas to the ions, denoted as “hydrodynamic” fraction. The main contribution of recoil energy results from the classical Coulomb repulsion, namely  $\sim 588$  eV.

Another possibility to explain the energy transfer is the thermal motion of the electrons that are bound to the assembly of ions. Their interaction would exert a pressure that we can call a “hydrodynamic” energy transfer. Evidence for the presence of this mechanism is provided by the directly opposed drop of electron kinetic energy starting at 150 fs, shown in the top panel of Figure 5. For the given simulation the ions gain approximately 22% of their kinetic energy due to the hydrodynamic expansion. Later we will show that the ratio between thermal expansion and the classical repulsion is very sensitive to the laser frequency. The electron-ion energy transfer has a larger influence on the dynamics if the excitation takes place off resonance.

### 3.4 Variable photon energy

To explore the dependence of the interaction dynamics on the photon energy we performed simulations for a range of laser frequencies, around the collective resonance. In Figure 9 results are shown for photon energies between 2.6–3.4 eV, from left to right, while the pulse shape and length as well as the peak intensity of  $I = 10^{11}$  W/cm<sup>2</sup> are kept constant. First we want to explain the features within the energy absorption and ionization. Therefore the phase angle between the laser field and the electronic dipole moment can serve as a key observable to understand the role of the collective excitation, shown in the bottom panels in Figure 9. For off-resonant excitations at  $\hbar\omega = 2.6$  eV and  $\hbar\omega = 3.4$  eV the dynamics are rather simple since the dipole moment follows the laser amplitude, plotted in black in the third row of Figure 9. Here the phase behaves similar to that of a classical damped oscillator. For the photon energies below and above the resonance the phase angle is close to zero and almost 180°, respectively. Both, the energy absorption and the ionization rate are small without much structure. Things



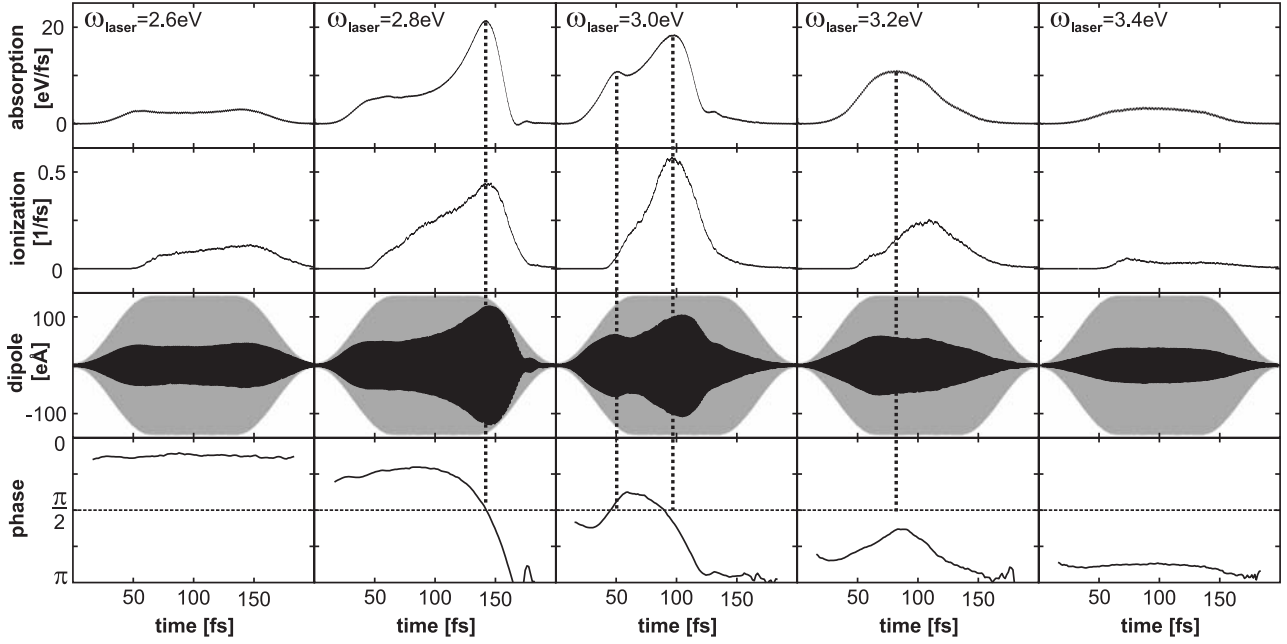


**Fig. 9.** Calculated excitations of  $\text{Na}_{147}$  for photon energies of  $\hbar\omega = 2.6\text{--}3.4$  eV from left to right. Each column corresponds to one simulation. Shown observables from top to bottom are the energy absorption, ionization rate, dipole signal and the dipole phase with respect to the driving laser. Within the plot of the dipole signal the pulse envelope is sketched in gray. Distinct peaks within the absorption are marked by dashed lines in order to guide the eye.

change dramatically when the photon energy is near resonance. The absorption and the ionization are significantly peaked, for  $\hbar\omega = 2.8\text{--}3.2$  eV, as may be seen in the first and second row in Figure 9. The energy shift of the collective excitation is responsible for the temporal change of the absorption. The progression with its distinct maxima can directly be compared to the evolution of the phase angle. For the example at  $\hbar\omega = 2.8$  eV, which has been discussed in the previous section, the plasmon energy is initially slightly above the photon energy and the phase angle is below  $90^\circ$ . As time evolves the phase angle first decreases somewhat, and then after  $t = 100$  fs it grows rapidly going through  $90^\circ$  and approaching  $180^\circ$  by the end of the laser pulse. In terms of the plasmon energy, a weak blue shift during the first period is followed by a strong red shift from the cluster explosion,  $\omega_{pl} \propto \sqrt{\rho_{ion}}$ . The small initial blue shift is associated with the ionization, which leaves a decreased electron density in the spill-out region. The effect is similar to the blue shift associated with cluster size; large clusters have a smaller proportion of electrons in the spill-out region. A near balance between the ionization-induced blue shift and the competing red shift due to the expansion can be found for the excitation at  $\hbar\omega = 3.0$  eV, shown in the center column of Figure 9. Here the plasmon is initially slightly below the photon energy, but the ionization effect yields a shift above the laser at about  $t = 50$  fs. At the crossing point a small peak appears in the energy absorption, marked with the first dashed line in this column. Some tens of femtoseconds later the compensating cluster expansion has lowered the plasmon energy leading to a second resonance roughly at  $t = 100$  fs. Here a strong peak occurs within the absorp-

tion signal while the ionization reaches its maximum too, second dashed line in the center column. After that second resonance the plasmon red shift dominates due to the fast expansion of the system. The phase quickly approaches  $180^\circ$  while the dipole amplitude decreases continuously. For the simulation at  $\hbar\omega = 3.2$  eV, the plasmon and photon energies never become equal. The consequences, seen in the figure, are an absence of sharp peaks in the absorption and a phase angle that does not go through  $90^\circ$ . Nevertheless the absorption has a broad maximum at  $t = 85$  fs where the frequencies almost match, indicated by a phase value that approaches  $90^\circ$ .

Comparing the results of all the simulations, one can see a systematic trend in when the maximum absorption occurs. Starting from  $\hbar\omega = 2.8$  eV, where the peak appears in the final phase of the laser pulse near  $\sim 150$  fs a continuous shift to earlier times can be observed with increasing photon energy. This behavior results from the tendency of the plasmon energy to decrease during the excitation if we ignore the influence of the ionization blue shift. Hence high photon energies support an early maximum while lower energies tend to a delayed optimum for the ionization by use of laser photon energies not too far away of the resonance.

### 3.5 Experimentally relevant data

In this section we examine some observables that are in principle accessible for experimental measurements, such as charge states and kinetic energies. In particular, we explore the influence of cluster size, considering clusters with

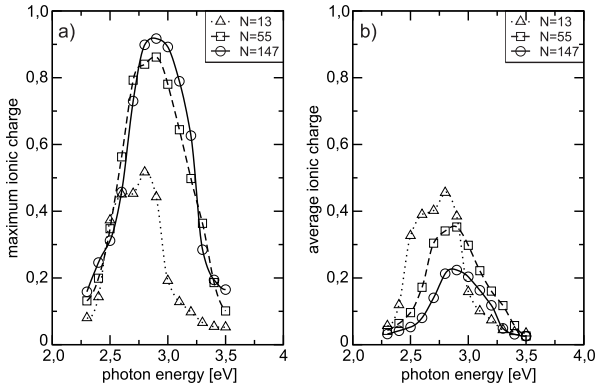


**Fig. 10.** Maximum (a) and average (b) charge of atomic fragments emerging from  $\text{Na}_N$  excited by a 200 fs laser pulse at  $I = 10^{11} \text{ W/cm}^2$ , for variable laser photon energy. The peak positions are near the plasmon energies for the particular cluster sizes. While the maximum charge state grows for larger clusters the average value decreases.

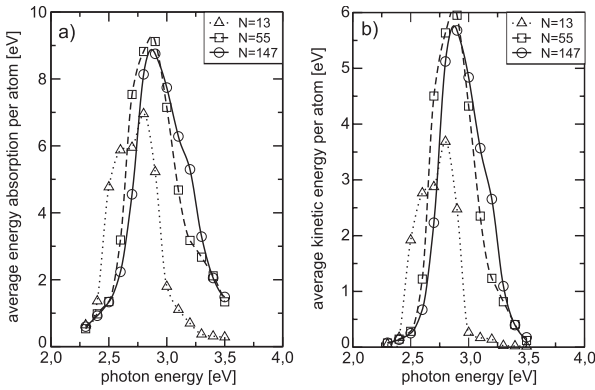


**Fig. 11.** Energy absorption (a) and average kinetic energy (b) of emitted ions after excitation of  $\text{Na}_N$ -cluster for variable laser photon energy. Note that the total energy is normalized with the cluster size.

$N = 13, 55$  and  $147$  atoms. The maximum and average charge states of atoms are shown in Figure 10 as a function of the photon energy. The curves all show a peak at the photon energy corresponding to the plasmon of the cold cluster. Another general trend is a growth of the maximum charge state with the size of the cluster in Figure 10a, while the inverse behavior is found for the average charge, as shown in the right panel.

To compare the energy absorption from the field and the release into recoil energy average values per atom are shown in Figure 11. Both, the total absorbed and the total ion kinetic energy are divided by the cluster size. According to the left panel the average absorbed energy per atom has a similar magnitude for  $\text{Na}_{55}$  and  $\text{Na}_{147}$  and a slightly smaller value in case of  $\text{Na}_{13}$ . This effect could be explained with the resonance enhancement, which seems to need a certain system size to reach full efficiency. The total released kinetic energy, shown on the right panel, in principle follows the total absorption, although the peak for  $\text{Na}_{13}$  is more suppressed than within the absorption. For laser frequencies near the plasmon resonance more

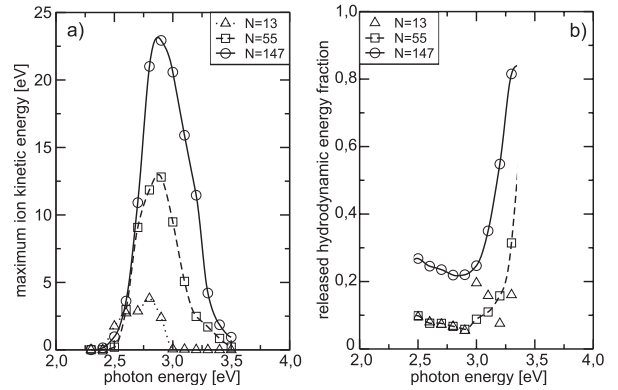


**Fig. 12.** Highest kinetic energy of released ions from the excitation of  $\text{Na}_N$ -cluster for variable laser photon energy (a). Fraction of kinetic energy release due to hydrodynamic forces of hot excited electron gas (b). Only data points of laser frequencies that induce a total cluster destruction are shown here.

than 50% of the power captured from the radiation field is transferred into ionic motion. Clearly the residual amount is needed for ionization and the break up of the metallic bond and remains as excitation within the electronic system.

The highest ion kinetic energy, however, strongly depends on the cluster size, shown in Figure 12a. A substantial increase in the maximum atomic recoil energy is found for bigger clusters. Here we find a roughly linear dependence of the peak energy with the cluster diameter, but a more extensive study would be necessary to confirm this scaling. This observation is in principle in agreement with our experimental studies on lead clusters [31].

A further question is the dominant source of repulsion within exploding clusters for different sizes. According to earlier theoretical investigations “hydrodynamic” effects play the leading role for very large clusters [6], while the pure Coulomb repulsion rules the expansion for smaller systems. In the present study the relaxation of energy is analyzed by comparing the Coulomb recoil energy with the electron-ion energy release according to Figure 8a. The fraction of the electron-ion energy release  $f_h$  can be resolved from the simulation, Figure 12b

$$f_h = 1 - \frac{E_{coulomb}}{E_{kin}}. \quad (9)$$

While in case of  $\text{Na}_{13}$  no clear result can be extracted from the data, a systematic behavior is found for the larger systems  $N = 55$  and  $N = 147$ . Obviously, with increasing size the electron-ion energy transfer is of growing importance. For all photon energies the fraction for  $\text{Na}_{147}$  is significantly higher than for  $\text{Na}_{55}$ . This is in accordance with the assumption above. With respect to the frequency dependence one finds a larger impact of the electron-ion energy transfer if the excitation is done off the plasmon frequency. Near the resonance a strong charging of the cluster emphasizes the pure Coulomb repulsion of the ions. Concerning the strong asymmetric graph in Figure 12b one has to mention, that the way of determination of  $f_h$  introduces a small overestimation of the relative fraction  $f_h$  for higher

photon energies. However, the major effect responsible for the asymmetry is the higher number of collisions that promotes effective electron-ion energy transfer for higher laser frequencies.

## 4 Discussion and conclusions

The TFV-MD model is practical for the dynamical description of simple metal clusters, in this work and in reference [12]. A necessary condition that must be satisfied is that the numerical algorithms have an accuracy to provide a stable ground state over a period of some picoseconds. We have seen here that the condition is achievable for clusters up to more than a hundred atoms, provided the atomic interaction is sufficiently smooth. This is certainly the case for the sodium clusters we have treated here, and we believe it will also be met for clusters of platinum or lead, taking a one-electron pseudopotential. Meeting the conditions for sodium, we found that the linear response of the system behaves very much as expected from quantum mechanical treatments. The transition strength is concentrated in a surface plasmon, whose frequency is red-shifted from the Mie value according to the well-known spillout effect, considering the ionization state and cluster size dependence. One difference we see with respect to quantal theories is that the semiclassical plasmon shows a damping associated with the electron-ion scattering on atomic pseudopotentials.

The response of the clusters in a strong field found to be controlled by simple considerations. In agreement with the conclusions of references [12, 32, 33], we found that the resonance condition between the plasmon and the laser field was crucial to obtain a high absorption. In detail, the plasmon frequency changes in time due to the ionization and expansion, so the resonance condition may only be satisfied after some time of irradiation. Evidence for this has been seen in experimental data references [4, 5]. We wish to emphasize that the mechanism is different to the enhanced ionization due to a critical interatomic distance [34], as proposed to be the leading process for rare gas clusters [9].

From the analysis of the simulated excitation of  $\text{Na}_{147}$  at  $\hbar\omega = 3.0$  eV we found a balance of the competing shift mechanisms of the plasmon, the ionic expansion and ionization. An indication for that has already been found in quantum TDLDA calculations on  $\text{Na}_{41}$  [33].

Following the laser pulse the ions undergo a Coulomb explosion, and we have presented a rather detailed picture of that phase of the dynamics. For absorption at resonance, the disassembly proceeds largely as a classical Coulomb explosion within the investigated size range, with the initial potential energy of the charged ion cloud converted to kinetic energy over the course of some hundreds of femtoseconds. Off resonance, the Coulomb potential energy is not enough to explain the energies of the final state. The electrons are thus involved in the energetics, perhaps providing pressure for a hydrodynamic expansion. As expected classically, the outer atoms are

the most ionized. Within a shell of atoms, there is an enhanced ionization of atoms facing the electric field axis. This suggests the field ionization mechanism plays some role.

A number of aspects of the dynamics depend on the cluster size. Of course the size-dependent blue shift of the plasmon is important for the resonance condition. Also, the maximum ionic charge state as well as the highest ionic recoil energy depend on cluster size, increasing with the number of atoms in the cluster. The trend for the recoil energy has also been observed in experiments [31, 35].

Our results are in principle agreement to data from reference [12], although we find a much stronger influence of the collective mode. The total ionization of the clusters is significantly higher in our calculations together with a more structured development of the absorption. Furthermore the shell structure of the clusters during the decomposition is much more stable in our model. These discrepancies are founded by the use of a different pseudopotential and test particle width as well as the implementation of another parametrization of the correlation effects. Nevertheless the contribution of energy transfer from hot electron to the ions due to scattering is very similar in both models.

So far the calculations have been performed with one active electron per atom participating in the dynamical propagation. The presented method is also applicable to other systems treated as single valence electron atoms. We are especially interested in the behavior of heavy metals with higher particle densities, like platinum or silver, to be subject to intense laser excitation. Furthermore we are preparing extensions to the model to allow the treatment of multiple electrons per atom.

We would like to thank P.-G. Reinhard and C. Guet for fruitful discussions. Financial support has been provided by the Sonderforschungsbereich 198, the Deutsche Forschungsgemeinschaft and the U.S. Department of Energy. Furthermore we like to thank the German "Verbund für Höchstleistungsrechnen Nord" (HLRN) for providing computer resources for the calculations.

## References

1. A. McPherson, B.D. Thompson, A.B. Borisov, K. Boyer, C.K. Rhodes, *Nature* **370**, 631 (1994)
2. E.M. Snyder, S.A. Buzza, A.W. Castleman Jr, *Phys. Rev. Lett.* **77**(16), 3347 (1996)
3. T. Ditmire, J.W.G. Tisch, E. Springate, M.B. Mason, N. Hay, J.P. Marangos, M.H.R. Hutchinson, *Phys. Rev. Lett.* **78**(14), 2732 (1997)
4. L. Köller, M. Schumacher, J. Köhn, S. Teuber, J. Tiggesbäumker, K.-H. Meiwes-Broer, *Phys. Rev. Lett.* **82**(19), 3783 (1999)
5. M.A. Lebeault, J. Viallon, J. Chevalyere, C. Ellert, D. Normand, M. Schmidt, O. Sublemontier, C. Guet, B. Huber, *Eur. Phys. J. D* **20**, 233 (2002)
6. T. Ditmire, T. Donnelly, A.M. Rubenchik, R.W. Falcone, M. Perry, *Phys. Rev. A* **53**(5), 3379 (1996)

7. T. Ditmire, R.A. Smith, J.W.G. Tisch, M.H.R. Hutchinson, *Phys. Rev. Lett.* **78**(16), 3121 (1997)
8. K. Ishikawa, Th. Blenski, *Phys. Rev. A* **62**, 063204 (2000)
9. Ch. Siedschlag, J.M. Rost, *Phys. Rev. Lett.* **89**(17), 173401-1 (2002)
10. L. Feret, E. Suraud, F. Calvayrac, P.-G. Reinhard, *J. Phys. B: At. Mol. Opt. Phys.* **29**, 4477 (1996)
11. C.A. Ullrich, A. Domsps, F. Calvayrac, E. Suraud, P.-G. Reinhard, *Z. Phys. D.* **40**, 265 (1997)
12. J. Daligault, C. Guet, *Phys. Rev. A* **64**, 043203 (2001)
13. E. Giglio, P.-G. Reinhard, E. Suraud, *J. Phys. B: At. Mol. Opt. Phys.* **34**, 253 (2001)
14. T.L. Beck, *Rev. Mod. Phys.* **72**(4), 1041 (2000)
15. E. Runge, E.K.U. Gross, *Phys. Rev. Lett.* **52**, 997 (1984)
16. O. Gunnarsson, B.I. Lundqvist, *Phys. Rev. B* **13**(10), 4274 (1976)
17. W.C. Swope, H.C. Andersen, P.H. Berens, K.R. Wilson, *J. Chem. Phys.* **76**, 637 (1982)
18. L.H. Thomas, *Proc. Camb. Phil. Soc.* **23**, 542 (1927)
19. E. Fermi, *Z. Phys.* **48**, 73 (1928)
20. E. Giglio, E. Suraud, P.-G. Reinhard, *Ann. Phys.* **11**(4), 291 (2002)
21. G.F. Bertsch, P.-G. Reinhard, E. Suraud, *Phys. Rev. C* **53**(3), 1440 (1996)
22. A. Domsps, P.-G. Reinhard, E. Suraud, *Ann. Phys.* **260**, 171 (1997)
23. A. Domsps, P.-G. Reinhard, E. Suraud, *Ann. Phys.* **280**, 211 (2000)
24. A. Domsps, P.-G. Reinhard, E. Suraud, *Phys. Rev. Lett.* **81**(25), 5524 (1998)
25. C. Jarzynski, G.F. Bertsch, *Phys. Rev. C* **53**(2), 1028 (1996)
26. *CRC Handbook of chemistry and physics* (CRC Press, 1987)
27. *Metal Clusters*, edited by Walter Ekardt (Wiley series in theoretical chemistry, 1998)
28. S. Kümmel, M. Brack, P.-G. Reinhard, *Phys. Rev. B* **62**(11), 7602 (2000)
29. J. Daligault, Ph.D. thesis, Lyon (2001)
30. I. Last, I. Schek, J. Jortner, *J. Chem. Phys.* **107**(17), 6685 (1997)
31. S. Teuber, T. Döppner, Th. Fennel, J. Tiggesbäumker, K.-H. Meiwes-Broer, *Eur. Phys. J. D* **16**, 59 (2001)
32. P.G. Reinhard, E. Suraud, *Appl. Phys. B* **73**, 401 (2001)
33. E. Suraud, P.G. Reinhard, *Phys. Rev. Lett.* **85**(11), 2296 (2000)
34. T. Seideman, M.Yu. Ivanov, P.B. Corkum, *Phys. Rev. Lett.* **75**(15), 2819 (1995)
35. T. Ditmire, E. Springate, J.W.G. Tisch, Y.L. Shao, M.B. Mason, N. Hay, J.P. Marangos, M.H.R. Hutchinson, *Phys. Rev. A* **57**(1), 369 (1998)